Research Square

Preprints are preliminary reports that have not undergone peer review.
They should not be considered conclusive, used to inform clinical practice,
or referenced by the media as validated information.

Boundary detection and turning-point reliability in gridded water– carbon products

Jingwen Wang[1]
Qilu Normal University
Xianzhi Wang[1]
Qilu Normal University
Duanguang Cao[1]
Qilu Normal University
Kang Pian[1]
Qilu Normal University
Yanying Wang[1]
20176917@qlnu.edu.cn

Qilu Normal University

Article

Keywords: evapotranspiration, vapour pressure deficit, gross primary productivity, nonlinear response surface, empirical support, model evaluation

Posted Date: November 19th, 2026

DOI: https://doi.org/10.21203/rs.3.rs-11571234/v1

License: This work is licensed under a Creative Commons Attribution 4.0 International License.
Read Full License

Additional Declarations: No competing interests reported.

Boundary detection and turning-point reliability in gridded water–carbon products

Jingwen Wang[1], Xianzhi Wang[1], Duanguang Cao[1], Kang Pian[1], Yanying Wang[1],*

[1] College of Geography and Tourism, Qilu Normal University, Jinan 250000, China

* Corresponding author: 20176917@qlnu.edu.cn (Y. Wang)

Tel.: +86-18053117135

Abstract

Gridded water–carbon products are used to infer transitions in vegetation responses to atmospheric dryness. We assessed the reliability of ET-conditioned VPD boundaries using eight-day PML evapotranspiration (ET) and gross primary productivity (GPP), together with ERA5-Land vapour pressure deficit (VPD), in Hetao croplands during 2019–2024. The observations represented 21,491 native PML cell–date units. Local boundaries persisted under equal source-unit weighting and single-record reconstruction. Correcting a prediction-basis inconsistency changed the turning geometry. All 1,000 block draws of the corrected weighted fit recovered a local boundary; 72.6% qualified an expansion–contraction turn, and the post-turn slope interval included zero. A separate spline refit also yielded an uncertain post-turn direction. Tests on 1,200 datasets with known boundaries showed that strict extraction reduced location error among qualified true turns while increasing missed and false turns. False-turn rates reached 42–44% for horizontal boundaries. Wetness-group comparisons were sensitive to eligibility within common support. Combining detection rates, conditional location error and block uncertainty provides a fuller assessment of transitions inferred from gridded products. In Hetao, the local response boundary was reproducible across the tested analyses, while the broader turning geometry remained uncertain.

Keywords: evapotranspiration; vapour pressure deficit; gross primary productivity; nonlinear response surface; empirical support; model evaluation

1. Introduction

Gridded evapotranspiration (ET) and gross primary productivity (GPP) products allow researchers to examine how vegetation carbon uptake varies with water use and atmospheric conditions. Nonlinear response surfaces can summarize these relationships through boundaries and turning points. The interpretation of such features depends on how consistently they can be recovered from the data. Evaluating the proposed feature directly complements the assessment of overall model performance (Gupta et al., 2012).

Vapour pressure deficit (VPD) is central to these water–carbon relationships. Increasing VPD raises evaporative demand, while stomatal regulation can reduce transpiration and CO_2 assimilation (Grossiord et al., 2020; Novick et al., 2016). Atmospheric dryness has been linked to lower vegetation growth and altered GPP and water-use efficiency (Yuan et al., 2019; Q. Zhang et al., 2019); crop simulations also identify yield losses beyond those explained by temperature (Hsiao et al., 2019). Soil moisture modifies production

stress (Liu et al., 2020), and the balance between evaporative demand and stomatal regulation can make ET rise or fall with VPD (Massmann et al., 2019). Joint ET–VPD analysis describes the water-flux states accompanying changes in carbon uptake.

At a fixed ET value, a positive-to-negative crossing of the fitted GPP derivative with respect to VPD defines a candidate boundary. Connecting these crossings across ET can produce a curve that rises and then falls. Boundary detection asks whether this sign change can be recovered consistently. Estimating a turn additionally requires enough connected points to establish the curve's direction on either side. Grouped resampling and tests with known turning and non-turning responses allow these aspects of reliability to be examined separately.

The structure of the source product also shapes the response. PML estimates ET and GPP jointly through coupled water and carbon calculations (Y. Zhang et al., 2019). It uses VPD to constrain GPP and links photosynthesis to canopy conductance and transpiration (He et al., 2022; Xu et al., 2026a). The fitted derivative therefore reflects environmental variation together with relationships built into the product. Repeatability measures how consistently that combined response is recovered.

Assigning a coarse product value to several finer analysis points gives it more fitting influence than a value assigned to fewer points. Shared meteorological forcing adds dependence. Equal weighting of native units, reconstruction of one record per unit and grouped resampling address different parts of this problem (Cameron and Miller, 2015). Validation must also account for spatial and temporal structure (Roberts et al., 2017). Boundary analysis therefore requires information about the source records and their coverage of the joint predictor domain.

Reproducibility in hydrology requires accessible data, code and execution instructions (Hutton et al., 2016; Stagge et al., 2019). For spline response surfaces, it also requires the training basis. Rebuilding the basis on a prediction grid can change the surface at the same physical coordinates, even when the fitted coefficients are retained. Saving the training basis preserves the fitted function and permits direct comparisons of support and extraction rules.

We use croplands in Hetao, western Inner Mongolia, as an empirical case. Irrigation and drainage sustain production in this dry environment and influence groundwater conditions and salt movement (Feng et al., 2005; Yu et al., 2010). The 2019–2024 panel combines PML ET and GPP with ERA5-Land meteorology (Muñoz-Sabater et al., 2021). We examine the local VPD-response boundary under alternative representations of these source observations.

We combine the Hetao analysis with experiments in which the response geometry is known. The empirical comparisons examine how source-unit representation and spline prediction affect the boundary, then quantify its stability under grouped resampling. The simulations evaluate true-turn detection, false detection and location error. Wetness groups and a low-GPP screening comparison examine how sample coverage

affects further comparisons. Together, these analyses assess the reliability of local boundaries and their estimated turns in gridded water–carbon products.

2. Data and methods

2.1. Study area

The Hetao Irrigation District lies along the upper Yellow River in western Inner Mongolia, China. Irrigation, drainage and shallow groundwater shape its agricultural water balance and salt redistribution (Feng et al., 2005; Ramos et al., 2023; Yu et al., 2010). We selected cropland observations within a study envelope formed by five county-level administrative units associated with Hetao (Figure 1) and pooled their ET–VPD–GPP records for response-surface analysis.

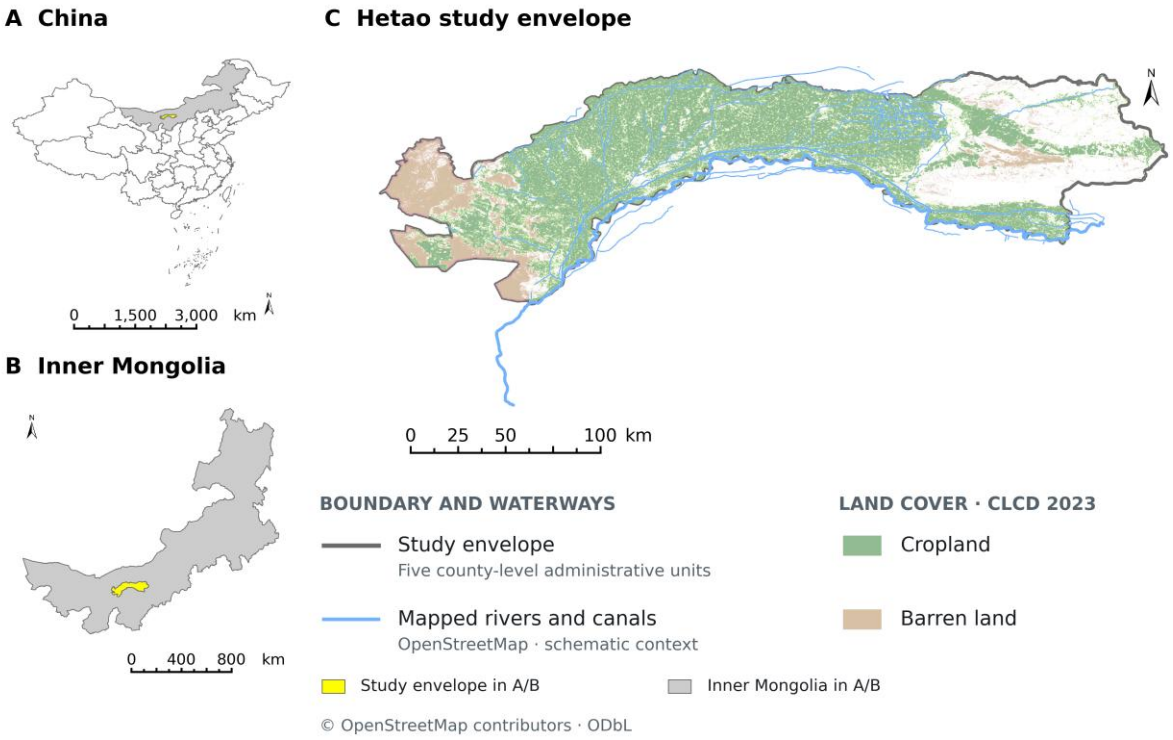


Figure 1. Geographic context of the Hetao study area. (A) Location in China. (B) Location within Inner Mongolia. (C) Land cover and schematic waterways. The dark outline combines the five county-level administrative units used to select observations. Yellow and grey in A/B identify the study envelope and Inner Mongolia, respectively. The background shows CLCD 2023 cropland and barren-land classes; the analytical cropland mask uses CLCD 2020. Rivers and canals are from OpenStreetMap (© OpenStreetMap contributors; ODbL).

2.2. Data and sample construction

ET and GPP were obtained from the MODIS branch of PML-V2.2a for 2019–2024 (Xu et al., 2026a, b). We used the 0.1° latitude–longitude NetCDF release, with 46 eight-day timestamps per year. ET and GPP are supplied as daily mean rates in mm d^{-1} and g C m^{-2} d^{-1}. We multiplied these rates by eight to obtain nominal eight-day totals and assigned the resulting ET_main and GPP_main values to one-kilometre analysis points from the nearest PML cell.

Cropland fraction was calculated from the 30-m Albers raster CLCD_v01_2020_albert.tif in the extended CLCD release (Yang and Huang, 2025), using class 1 for cropland. For each analysis point, we calculated the fraction of cropland pixels within an approximately one-kilometre window. The initial grid skeleton required a fraction of at least 0.30; the fitting sample required at least 0.50. The original CLCD study documents the classification method (Yang and Huang, 2021), while the extended release supplies the 2020 raster.

Table 1. Data products, native support, and roles in the analysis.

Source / period	Analytical variable	Role and qualification
PML-V2.2a MODIS branch, 2019–2024; 0.1° NetCDF, eight-day	ET_main; GPP_main	Daily mean ET and GPP rates × 8; nearest-cell assignment to 1-km grid points.
ERA5-Land hourly meteorology, 2019–2024	VPD_mean; VPD_max; swvl4 (DSWI); cell identity	Eight-day mean VPD for fitting; hourly-window maximum for baseline screening; layer-4 soil water (100–289 cm) for subgroup analysis.
CLCD v01 2020; 30-m Albers raster	Cropland fraction	Class 1 fraction in an approximately 1-km window; initial ≥ 0.30, final ≥ 0.50.
MOD16 Terra / MYD16 Aqua ET and VPM GPP, 2001–2016 or 2002–2016	ET; VPM GPP	Archival implementation provenance; derivative and frontier results excluded because grid-axis ordering is unresolved.

Hourly VPD was calculated from ERA5-Land 2-m air temperature T and dew-point temperature Td, both in °C, using the saturation-vapour-pressure difference in Eq. (1) (Allen et al., 1998; Muñoz-Sabater et al., 2021). Within each year, hourly values were averaged over eight-day windows beginning on 1 January. This mean, VPD_mean, was the predictor in every response-surface fit. The maximum hourly VPD in each window, VPD_max, entered the original complete-case screen only. Both variables were assigned to the analysis points from the nearest 0.1° ERA5-Land cell.

$$\mathrm{VPD}_h = 0.6108\exp\left(\frac{17.27T_h}{T_h + 237.3}\right) - 0.6108\exp\left(\frac{17.27T_{d,h}}{T_{d,h} + 237.3}\right) \quad (1)$$

DSWI was the ERA5-Land layer-4 volumetric soil-water variable swvl4, expressed in $m^3\ m^{-3}$ and representing 100–289 cm depth (Muñoz-Sabater et al., 2021). We averaged hourly values over the year-specific eight-day windows used for VPD. DSWI served as the deep-layer wetness proxy in the subgroup analysis.

The initial panel contained 3,323,316 records. Restriction to April–October, cropland fraction ≥0.50 and complete key fields retained 1,737,842 records. The original complete-case screen included GPP_main, ET_main, VPD_max, swvl1 and swvl2; both VPD variables were complete in the final sample. Excluding GPP_main values at or below the twentieth percentile (P20; 4.24 g C m^{-2} per 8 d) left 1,379,769 records.

We retained the existing random sample of 200,000 rows, drawn with seed 42, for all same-panel comparisons. It covered 10,887 one-kilometre locations with unique location–eight-day keys.

Nearest-neighbour linkage identified 202 ERA5-Land cells and 1,207 meteorological cell×year units during 2019–2024. These identifiers defined the meteorological blocks used in the uncertainty analysis (Cameron and Miller, 2015).

Reconstructing the original PML assignment identified 193 source cells, 1,145 PML cell×year units and 21,491 cell×eight-day ET/GPP records. Values agreed within every source cell–date unit. We examined two alternative representations. In the weighted analysis, each nominal row received weight 1/n, where n was its cell–date multiplicity, giving every source unit equal total fitting weight. In the single-record analysis, we retained one ET/GPP record per PML cell–date. Meteorology was assigned at the PML-cell centre from the nearest ERA5-Land cell, using the same hourly-to-eight-day aggregation. This produced a source-unit panel with a consistent geographical assignment rule.

2.3. Response surfaces and boundary extraction

We fitted cubic B-spline response surfaces to ET_main, VPD_mean and their tensor-product interaction by ordinary least squares. The original model used six degrees of freedom per predictor and is labelled df6 throughout. Its baseline extractor retained the first permitted positive-to-negative VPD-derivative crossing in each ET column under a histogram density mask. We reproduced its fixed-sample turn and original 200 row-wise bootstrap replicates, reporting the fixed-sample estimate, bootstrap mean and percentile interval separately.

We compared the archived df6 predictions, which rebuilt the basis on the strict evaluation grid, with predictions that reused the saved training basis. The controlled comparison supplied the same physical grid and derivative field to both extractors. A separate df7×df7 model was refitted to the frozen observations with an explicitly specified spline state. Figure 2 distinguishes the historical calculations, paired extraction controls and separate refit.

Training-basis predictions were constructed with Patsy's build_design_matrices and the saved DesignInfo, retaining knots, boundaries, transformations, intercept and column order (Patsy developers, n.d.). We checked predictions at matched coordinates when evaluated individually, in batches and over changed coordinate ranges. The tolerances were 10^{-8} for GPP and 10^{-6} for its VPD derivative. A central-difference step of 10^{-4} kPa was used for this consistency check. Extraction itself used the numerical derivative on the evaluation grid, with points outside the training boundaries treated as unevaluable.

The paired df6 extractors differed in their support and curve-selection rules. The legacy extractor used histogram count >5, the first positive-to-negative crossing per ET column and at least five points on each side of a candidate turn. The strict extractor used the local-support, connectivity and ten-points-per-side rules defined below. Within each paired comparison, both received the same fitted surface, physical grid and derivative field.

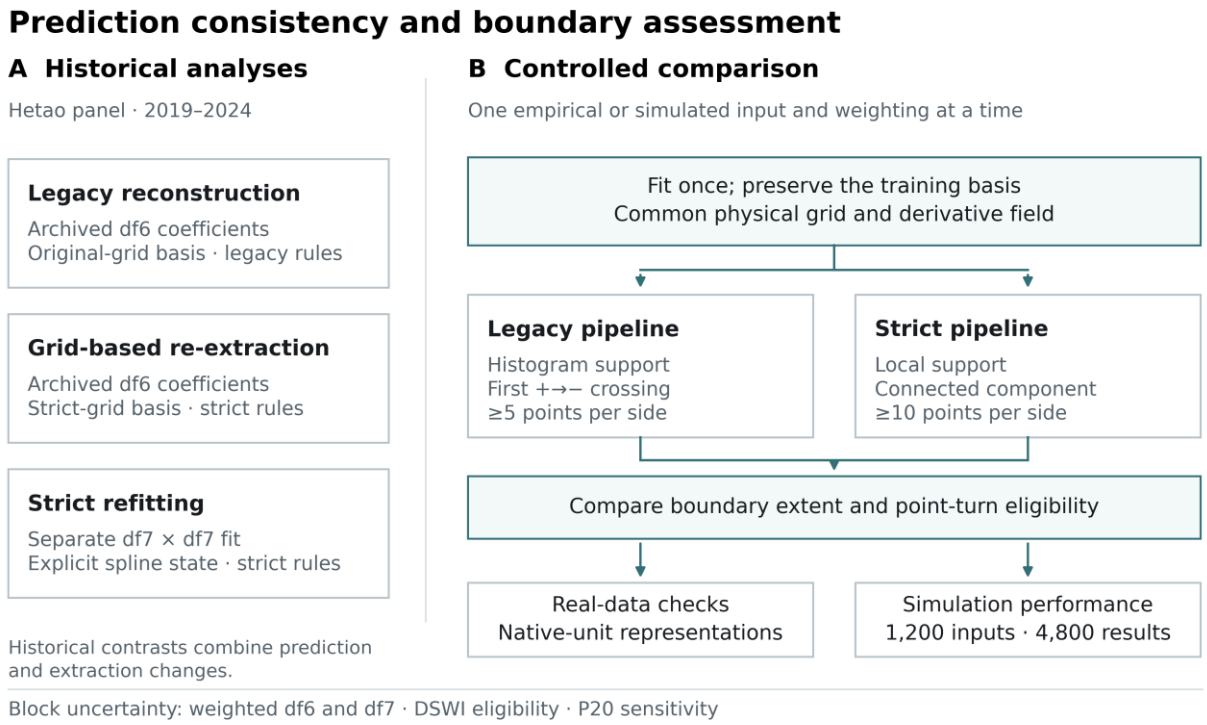


Figure 2. Design of the boundary assessment. (A) Historical calculations on the frozen Hetao panel: baseline df6, archived df6 evaluated with a rebuilt basis on the strict grid, and a separate df7×df7 refit with fixed spline state. (B) Controlled df6 comparisons share the training fit, saved basis, physical grid and derivative field before applying the legacy and strict support and extraction rules. Evaluation combines the empirical native-unit representations with 1,200 known-boundary datasets, yielding 4,800 simulation results. Block resampling assesses the corrected weighted df6 and df7 fits; wetness groups and the P20 comparison provide additional sensitivity assessments.

We evaluated ET and VPD_mean on a 100 × 100 grid spanning the frozen sample's 2.5th–97.5th percentile rectangle. Both axes were scaled to the unit interval when calculating neighbourhood support. At node (e, v), Nr is the number of nominal records within radius r, and Ncell and Nyear are the numbers of distinct ERA5-Land cells and years. The strict support rule required r = 0.05, Nr ≥ 50, Ncell ≥ 5 and Nyear ≥ 3 (Eq. 2). These criteria were fixed for the reassessment after the baseline analysis. The weighted fit used the same nominal-record support mask, allowing fitting weights to change while retaining the support-counting rule.

$$S(e,v) = \mathbf{1}(N_r \geq 50)\,\mathbf{1}(N_{\text{cell}} \geq 5)\,\mathbf{1}\big(N_{\text{year}} \geq 3\big), \quad r = 0.05 \tag{2}$$

At supported nodes, we calculated D(e, v), the fitted GPP derivative with respect to VPD_mean. Linear interpolation located positive-to-negative crossings between adjacent VPD nodes (Eq. 3). Crossings in consecutive ET columns belonged to the same component when their VPD bracket indices differed by at most one. A missing column or larger jump ended the component. This rule defined the connected candidate boundaries.

$$D(e,v) = \frac{\partial \hat{g}(e,v)}{\partial v}, \quad \hat{v}_0 = v_k - \frac{D(e,v_k)}{D(e,v_{k+1}) - D(e,v_k)}\,(v_{k+1} - v_k) \tag{3}$$

We selected the component F with the widest ET span, resolving ties by its number of represented ET columns and then crossings. In Eq. (4), e_F^{max} and e_F^{min} are its extreme ET coordinates; e_S^{max} and e_S^{min} are the extremes of distinct ET columns containing qualified nodes. CF is their span ratio. The denominator includes any internal gaps between qualified columns, so the metric describes overall ET extent rather than continuously observed interval length. The distinct-column ratio was recorded separately. Empty or zero-span qualified domains are non-evaluable; empty-component flags retain each source procedure's convention.

$$C_F = \frac{e_F^{max} - e_F^{min}}{e_S^{max} - e_S^{min}} \tag{4}$$

The separate df7 refit used cubic B-spline bases with internal knots at the twentieth, fortieth, sixtieth and eightieth percentiles of each predictor. Bj(e) and Ck(v) denote the seven ET and VPD basis columns. The surface in Eq. (5) contained an intercept, seven terms for each predictor and 49 interactions, giving 64 design columns. This specification changed the fitted surface while retaining the frozen response and predictor records (Wood, 2017).

$$\hat{g}(e, v) = \beta_0 + \sum_{j=1}^{7} a_j B_j(e) + \sum_{k=1}^{7} c_k C_k(v) + \sum_{j=1}^{7}\sum_{k=1}^{7} d_{jk} B_j(e) C_k(v) \tag{5}$$

We fitted a continuous two-slope function to boundary VPD along the selected component (Eq. 6). Candidate turns had to lie within the central 80% of the supported ET span. The primary strict rule required at least ten selected points strictly on each side; because the candidate was excluded from both counts, at least 21 points were needed. An expansion–contraction turn also required a positive pre-turn slope and a negative post-turn slope (Eq. 7). Slopes are expressed in kPa per (mm per 8 d). We retained numerical turning locations and recorded whether each satisfied the full rule.

$$v_F(e) = \alpha + \beta_{\text{pre}}(e - \tau), \quad e \leq \tau \tag{6}$$

$$v_F(e) = \alpha + \beta_{\text{post}}(e - \tau), \quad e > \tau$$

$$\beta_{\text{pre}} > 0, \qquad \beta_{\text{post}} < 0 \tag{7}$$

2.4. Uncertainty and evaluation

For the corrected, saved-training-basis df6 fit with equal native-unit weights, we performed 1,000 ERA5-Land cell×year block draws from the 1,207 blocks, using PCG64 seed 20261026. Each draw sampled 1,207 blocks with replacement and multiplied each row's fixed inverse-multiplicity weight by the number of times its block was selected. We refitted the coefficients while retaining the training basis, evaluation grid and base support mask. Slope percentiles used all finite candidates meeting the interior and side-count

requirements. Qualification additionally required opposing slope signs. Turning locations were summarized for all numerical candidates and for the qualified subset separately.

For the nominal-row df7 fit, we used 1,000 ERA5-Land cell×year draws. The weighted df7 fit used 1,000 ERA5-Land and 1,000 PML cell×year draws, grouping shared meteorology and product histories, respectively. These draws likewise refitted coefficients and recalculated crossings, component selection and slopes under fixed spline state, grid and base support. Percentile intervals therefore condition on the retained support. The historical row bootstrap regenerated its prediction basis and histogram support.

To assess the P20 screen, we compared two separately sampled 200,000-row panels on their own and common qualified domains (Supplementary Table S1). One retained the GPP screen; the other was drawn from the 1,737,842 complete records before screening. This comparison jointly changes sample composition and predictor support. We evaluated its point geometry without additional block resampling.

The DSWI analysis used 196,243 rows after restricting ET to its first–ninety-ninth percentile range. Low and high groups comprised values at or below the fortieth percentile and at or above the sixtieth percentile of DSWI. We estimated displacement, $\Delta\tau = \tau\text{high} - \tau\text{low}$, when both groups qualified within the intersection of their support masks. The main rule required ten points strictly on each side of a turn. A post-hoc sensitivity reduced this minimum to eight, retaining the fitted surfaces and all other support, connectivity and slope-sign criteria. We performed 1,000 paired ERA5 cell×year draws for this sensitivity and reported the number in which both groups qualified. Draws without a qualified pair remained in the eligibility denominator and had no assigned displacement.

The known-boundary experiments combined four prescribed response functions, three sampling conditions and 100 frozen seeds per combination, producing 1,200 datasets. The functions described an expansion–contraction boundary (A), a monotonic boundary (B), a horizontal boundary (C) and no boundary (D). Each dataset was analysed with both df6 extractors under nominal multiplicity and equal native-unit weighting. The resulting 4,800 control results came from paired comparisons sharing the training fit, saved basis, physical grid and derivative field. The simulated datasets were analysed without P20 screening.

Before support deletion, each simulated dataset contained 193 native cells, six years and 21,491 cell–date records. Predictors were stratified across normalized ET–VPD space. Multiplicity increased with normalized ET, with replicated records retaining their predictor values, GPP and generated errors. The sparse condition retained 19 cells within $x = 0.45$–0.55. The deleted-band condition removed $x = 0.48$–0.52; its width was smaller than the support-neighbourhood diameter of 0.10. Native and meteorological cell identities coincided in these experiments.

We evaluated turn qualification, false detection and conditional turn-location error. Each detection rate used all 100 attempts in its truth–support–extractor–weighting combination. Mean absolute location error used qualified true-turn estimates, with their count reported alongside the detection rate. Rates received Wilson binomial intervals. Paired comparisons used identical seeds and shared derivative fields. Boundary

detection required a component with positive ET span; turn qualification was assessed separately. These controls evaluated point detection without new interval draws. Twelve saved native tables matched exactly; the remaining datasets were regenerated from the frozen generators and seeds and checked against archived multiplicity and fit diagnostics.

We also examined the archived MOD16 Terra/MYD16 Aqua ET and VPM GPP calculations (Mu et al., 2011; Xiao et al., 2004). Their prediction matrix used ET-major ordering, whereas derivative and support operations treated the first axis as VPD. We excluded the affected derivative fields, crossings and coefficient-draw summaries from the product comparison. The empirical evidence presented here therefore concerns PML.

We summarized geographical support at the native PML-cell scale, mapping the number of distinct cell–date observations and the fraction of assigned records within qualified ET–VPD support. Each predictor pair was linked to the nearest evaluation-grid node. We calculated support fractions within cell–date and averaged them equally across dates. The supplementary derivative-sign map used the same date weighting. These maps locate the observations and predictor states contributing to the shared fitted surface.

3. Results

3.1. Native observations define an unevenly sampled predictor domain

The frozen panel contained 200,000 assigned eight-day rows at 10,887 one-kilometre locations. These represented 193 native PML cells, 202 ERA5-Land cells and 21,491 distinct PML cell–date ET/GPP units (Table 1). The distinction between assigned rows and source units was substantial: each ET/GPP unit appeared in 1–28 rows, with a median multiplicity of nine.

ET and GPP values agreed within every reconstructed source unit. Repeated fine-grid assignment gave the units unequal fitting influence, which equal source-unit weights removed. The single-record reconstruction also assigned meteorology at each PML-cell centre.

The geographical distribution of observations was uneven (Figure 3A). PML cells contributed 3–156 distinct eight-day dates, with a median of 119; seven cells contributed fewer than 20. The date-averaged fraction of assigned ET–VPD states within qualified support had a median of 0.918 and 10th and 90th percentiles of 0.840 and 0.953 (Figure 3B). Most sampled states therefore lay within the qualified domain, although temporal representation varied among cells. The supplementary derivative-sign map showed weak spatial differentiation and is retained as a diagnostic (Supplementary Figure S2).

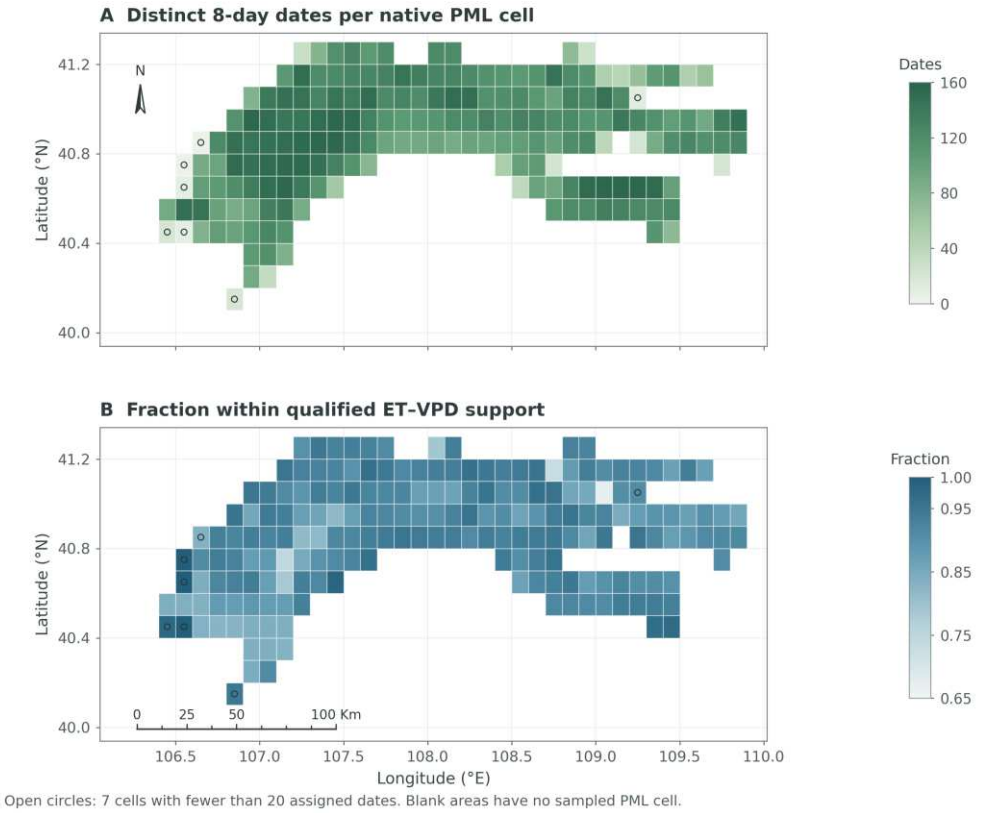


Figure 3. Geographic support at the native 0.1° PML scale. (A) Distinct cell×eight-day dates, totalling 21,491 across 193 cells. (B) Fraction of assigned records within qualified ET–VPD support, calculated within each cell×date and averaged equally across dates. Open circles identify seven cells with fewer than 20 dates; blank areas contain no sampled native cell. Panel B summarizes support for the pooled response surface. Its blue scale spans 0.65–1.00, and the shared 100-km scale bar appears in B.

The strict evaluation grid covered ET of 1.84–35.12 mm per 8 d and VPD of 0.532–2.684 kPa. Of its 10,000 nodes, 8,951 met the local record, meteorological-cell and year requirements. Figure 4A shows these states alongside the nominal record density. Several separate candidate branches appeared within the qualified domain (Figures 4B and 5).

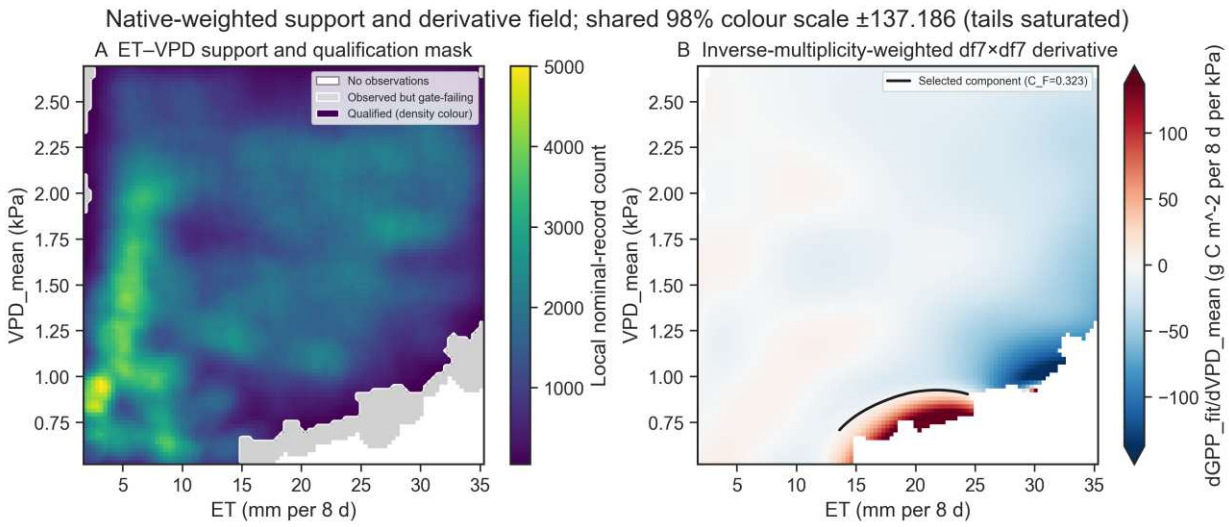


Figure 4. Empirical support and boundary selection in the df7 analysis with inverse-multiplicity weights. (A) Local nominal-record density: white denotes no observations, grey denotes observed nodes failing a support criterion, and colour denotes qualified nodes. (B) Fitted VPD derivative and the selected boundary, whose ET-span ratio CF is 0.323. Figures 4B and 5A/B share a zero-centred RdBu_r scale of ±137.186 g C m^{-2} per 8 d per kPa, set by the pooled 98th percentile of absolute qualified-node derivatives. Endpoint colours saturate 22 lower-tail and 46 upper-tail nodes in B. Grey and blank regions have no qualified derivative estimate.

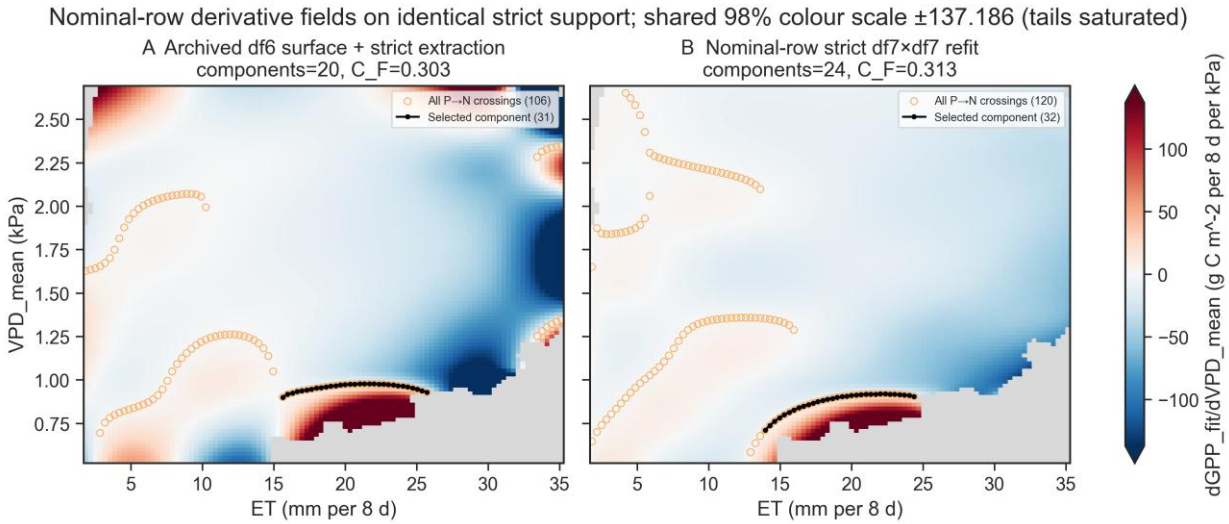


Figure 5. Nominal-row PML derivative fields in the archived df6 and separate df7 analyses. (A) Archived df6 coefficients evaluated with the basis rebuilt on the strict grid. (B) The df7×df7 refit with fixed spline state. Orange circles identify all positive-to-negative crossings (106 and 120); black points identify the selected components (31 and 32). Their ET-span ratios CF are 0.303 and 0.313. The panels share the support mask and colour scale used in Figure 4B. Grey denotes unqualified support. Colours saturate at 266 lower-tail/143 upper-tail nodes in A and 0 lower-tail/61 upper-tail nodes in B; numerical derivatives are retained in full.

3.2. A local boundary persists while its post-turn direction remains uncertain

The nominal-row df7 refit returned 120 crossings in 24 components. The selected component contained 32 points and spanned 10.42 mm per 8 d, giving CF = 0.313 (Figure 5B). Its numerical turn was 17.98 mm per 8 d, with pre- and post-turn slopes of 0.04137 and +0.00326 kPa per (mm per 8 d). The positive post-turn

slope failed the expansion–contraction rule. All 1,000 ERA5 cell×year block draws selected a boundary, but the post-turn slope interval extended from −0.00637 to 0.00698; 839 draws had positive slopes (Figure 6D–F).

Both native-unit representations retained a local component in the df7 fit (Table 2). Equal weighting yielded 8,951 qualified nodes and a 33-point component with CF = 0.323. Single-record reconstruction yielded 8,125 nodes and a 36-point component with CF = 0.354.

Both block schemes recovered a boundary in every weighted df7 draw. Median CF was 0.333 across each set of 1,000 draws. Its 2.5th–97.5th percentile range was 0.293–0.364 for ERA5 blocks and 0.283–0.374 for PML blocks. Post-turn slope ranges were −0.0080 to 0.0070 and −0.0104 to 0.0074 kPa per (mm per 8 d), respectively. The two grouping schemes therefore agreed on a recurring local component and an uncertain post-turn direction within the retained base support.

Table 2. Point results for the df7 fit under alternative PML counting units. CF is the selected-component ET span divided by the overall qualified ET span. The single-record analysis assigns meteorology at PML-cell centres. Block intervals for the weighted analysis appear in Section 3.2; the single-record analysis provides point estimates.

Strict refit	Rows	Qualified nodes	Crossings / components	Selected points	ET-span ratio C_F
Nominal rows	200,000	8,951	120 / 24	32	0.313
Inverse-multiplicity weighting	200,000	8,951	127 / 24	33	0.323
One record per PML cell×date	21,491	8,125	121 / 20	36	0.354

The P20 comparison changed the estimated point geometry (Supplementary Table S1). Without screening, CF on the sample's own domain was 0.242, and the common-support turn at 11.5887 mm per 8 d passed the point criteria. With P20 retained, the common-support numerical turn was 18.6481 mm per 8 d, with a positive post-turn slope. These results describe the joint sensitivity to composition and support in the two separately sampled panels.

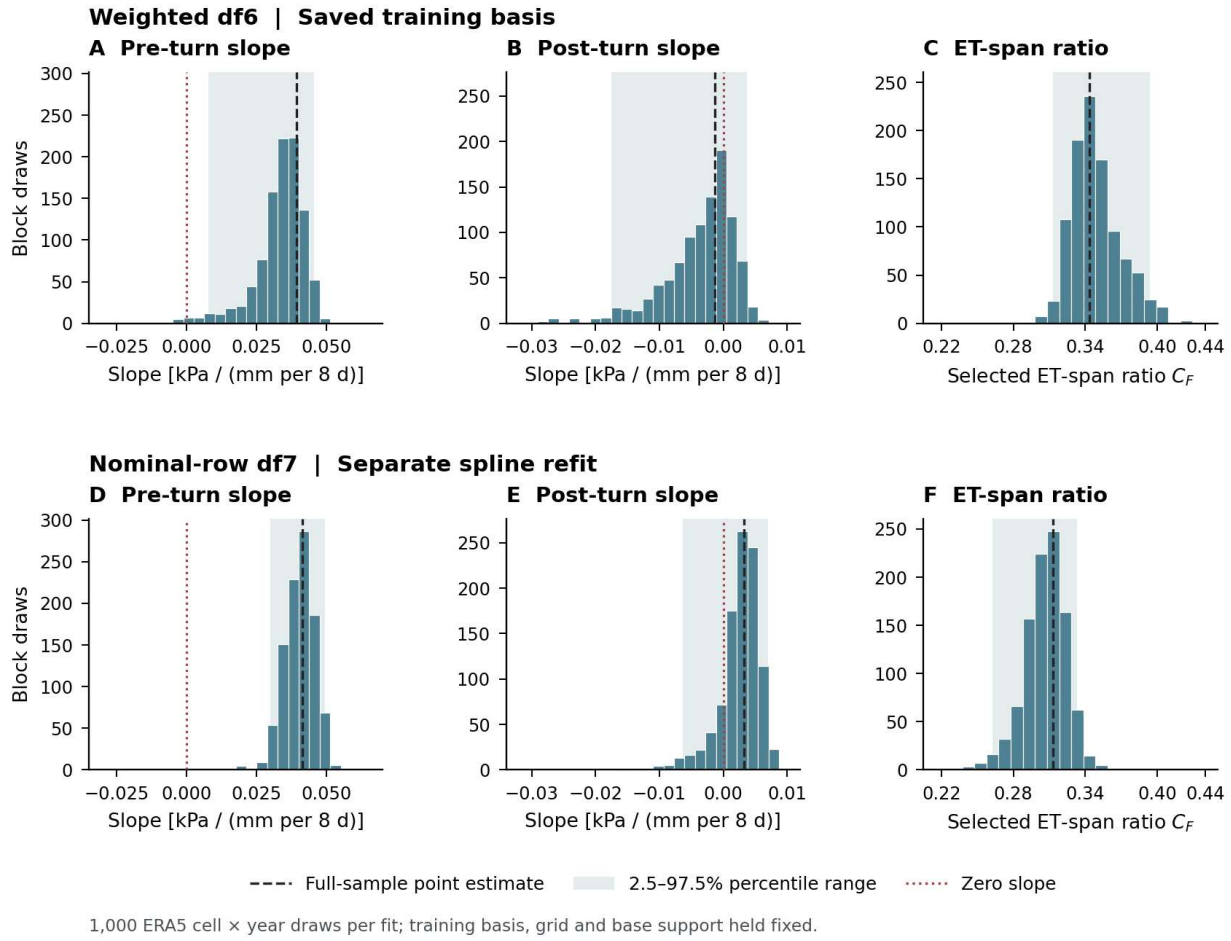


Figure 6. Block-resampling uncertainty in the corrected weighted df6 fit (A–C) and the separate nominal-row df7 refit (D–F). Columns show pre-turn slope, post-turn slope and selected-component ET-span ratio CF. Each row summarizes 1,000 ERA5-Land cell×year draws and retains its own spline specification and record weighting. Dashed lines show the reported full-sample point estimates; shaded bands show the empirical 2.5th–97.5th percentiles, and dotted red lines mark zero slope. Slope distributions include all finite interior candidates, irrespective of their signs. The weighted df6 turn qualified in 726 draws; the nominal-row df7 post-turn slope was positive in 839 draws. Training basis, evaluation grid and base support remained fixed within each analysis. Supplementary Table S4 gives the two df6 turning-location distributions.

3.3. Prediction consistency changes the inferred turning geometry

The historical baseline yielded a fixed-sample turn of 13.4012 mm per 8 d from 46 crossings. Across its 200 row-wise bootstrap replicates, the mean was 12.9796 (reported as 12.98), with a percentile interval of 12.4897–13.8570. Evaluating the archived df6 coefficients with a basis rebuilt on the strict grid instead yielded 106 crossings in 20 components. The selected 31-point component had CF = 0.303, an ET span of 10.08 mm per 8 d and a numerical turn at 21.00 mm per 8 d, with slopes of 0.01326 and −0.00986 (Figure 5A). Because the prediction bases were rebuilt, this historical contrast combines a change in the evaluated surface with a change in extraction rules.

Preserving the training basis recovered local components under all three record representations (Table 3). Strict extraction selected 33 nominal-row, 35 weighted and 34 single-record points, with CF values of 0.323232, 0.343434 and 0.333333. The corresponding point turns were 17.3034, 16.9673 and 16.9745 mm

per 8 d. Each passed the opposing-slope and side-count criteria. The weighted and single-record estimates were close, whereas their geometry differed from that obtained by rebuilding the prediction basis.

Table 3. Point results from strict extraction of the df6 surface evaluated with its saved training basis. All representations use the shared physical grid and pass the point qualification rule. CF measures ET span; the distinct-column ratio is listed separately. βpre and βpost are expressed in kPa per (mm per 8 d). Block-resampling results for the equal native-unit-weighted arm appear in Figure 6A–C, Section 3.3 and Supplementary Table S4.

Analysis arm	Crossings / components	Selected points	C_F	Column ratio	τ (mm/8 d)	βpre	βpost
Nominal rows	83 / 19	33	0.323232	0.33	17.303434	0.034186	−0.003998
Equal native-unit weights	88 / 19	35	0.343434	0.35	16.967272	0.039160	−0.001349
One record per PML cell×date	87 / 20	34	0.333333	0.34	16.974545	0.042033	−0.001368

The basis change altered predictions well inside shared support. Across 8,816 shared internal nodes, the median absolute GPP difference was 5.50786 g C m^{-2} per 8 d. The median difference in the fixed-step VPD derivative was 5.79026 g C m^{-2} per 8 d per kPa, with opposite signs at 1,543 nodes. Reusing the saved training state restored agreement at matched coordinates. On the shared grid and derivative field, the legacy extractor failed the opposing-slope rule for nominal and weighted records, while strict extraction passed it; the single-record legacy extractor selected an earlier local turn. This paired comparison isolates the support and extraction pipelines from the prediction-basis change.

The corrected weighted df6 fit recovered a boundary and an interior numerical candidate in all 1,000 block draws (Figure 6A–C). The median CF was 0.343434, with a 2.5th–97.5th percentile range of 0.313131–0.393939. The corresponding slope ranges were 0.007683–0.045544 before the turn and −0.017526–0.003655 after it, each based on all 1,000 candidates. Expansion–contraction geometry qualified in 726 draws (72.6%). Boundary occurrence was consistent across draws, while the direction of the post-turn segment varied.

Across all 1,000 numerical candidates, τ had a median of 17.3034 mm per 8 d and a 2.5th–97.5th percentile range of 16.6311–19.3204. Among the 726 qualified turns, the median was 17.6396 and the range was 16.6311–19.2784 mm per 8 d. Supplementary Table S4 reports both distributions with their eligibility counts.

3.4. Lower conditional location error accompanies more detection errors

Figure 7 evaluates qualification and location error together. Strict extraction qualified true turns in 95–98% of nominal and 93–98% of weighted attempts, compared with 99–100% for legacy extraction (Figure 7A). Among the qualified cases, strict extraction had lower mean absolute location errors: 1.316–1.847 mm per 8 d for nominal and 1.391–1.828 for weighted records, compared with legacy ranges of 1.418–2.127 and 1.557–2.116 (Figure 7B; Supplementary Table S3). These ranges span the three support conditions. The

lower error describes accepted true turns; strict extraction still missed two to seven of every 100 true-turn attempts, compared with zero or one for the legacy extractor.

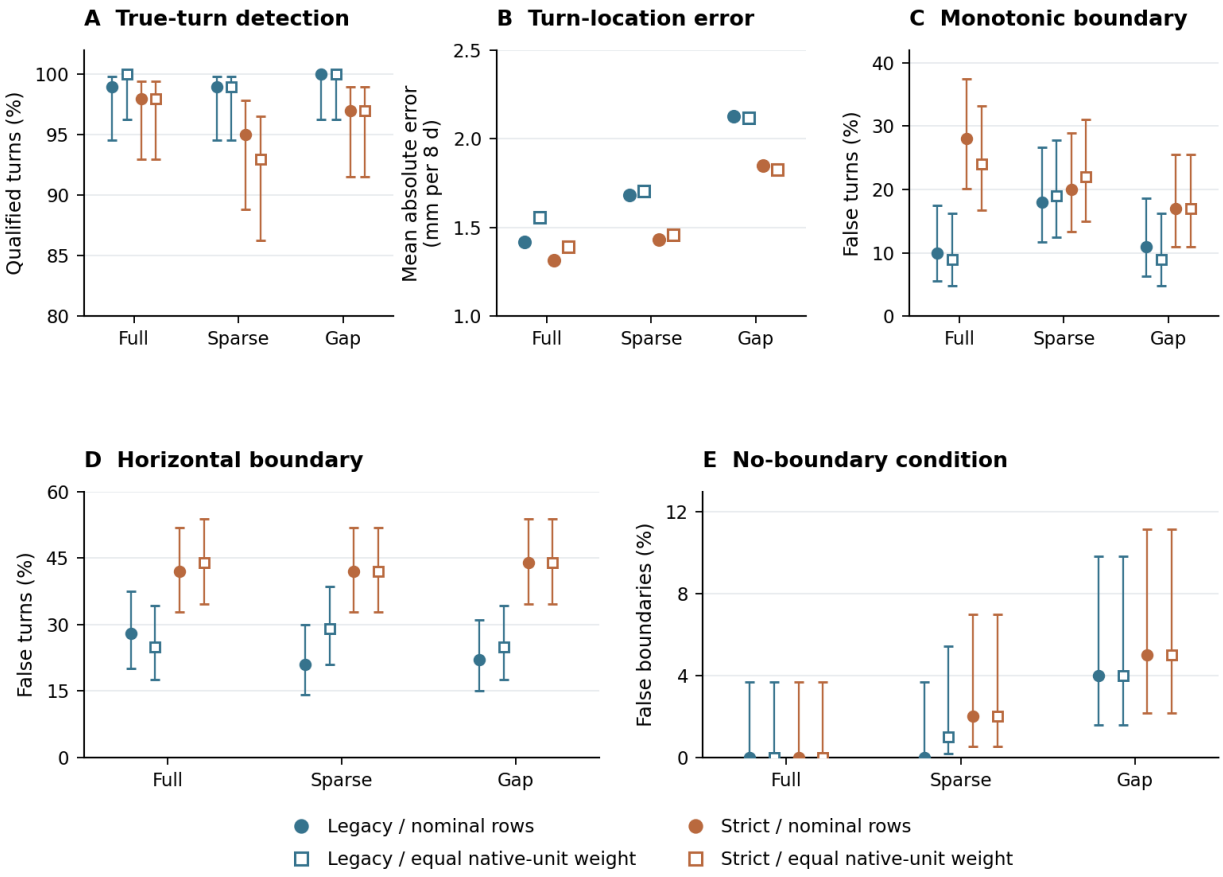


Figure 7. Detection and localization in the known-boundary experiments. Both df6 extractors use the saved training basis and share the physical grid and derivative field within each weighting. (A) Qualified true turns. (B) Mean absolute turn-location error among qualified true-turn cases. (C–D) False turns on monotonic and horizontal boundaries. (E) Selection of a positive-span component when no boundary exists. Every rate uses all 100 attempts; bars show 95% Wilson binomial intervals. Panel B has no uncertainty bars and uses the qualified count represented by each corresponding percentage in A. Colour identifies the extractor; filled circles and open squares identify nominal-row and equal native-unit weighting. Full, sparse and gap denote full sampling, sparse sampling and the deleted-band condition; the gap can be bridged by the support neighbourhood. No-boundary false-turn counts were 0/100 in every condition, separately from the component rates in E.

False-turn rates increased under strict extraction. Monotonic boundaries yielded qualified turns in 17–28% of strict and 9–19% of legacy attempts (Figure 7C). Horizontal boundaries yielded rates of 42–44% and 21–29%, respectively (Figure 7D). When no boundary existed, the procedures selected positive-span components in 0–5% of strict and 0–4% of legacy attempts (Figure 7E), while neither returned a false turn in any 100-attempt condition. Supplementary Table S2 gives the denominators and Wilson intervals, including nonzero upper limits for zero-event cases. The gain in conditional location accuracy was accompanied by lower true-turn detection and higher false-turn rates.

3.5. Wetness-group displacement is sensitive to turning eligibility

The original DSWI analysis returned turns of 7.18 and 9.35 mm per 8 d, a high-minus-low difference of +2.17. The reassessment used the 196,243-row ET P1–P99 sample, with low and high wetness cutoffs of ≤0.133545 and ≥0.134375. Both groups qualified on their own domains, with turns at 12.83 and 21.29 mm per 8 d (Table 4). The common domain contained 8,128 qualified nodes. The low group retained its 12.83 turn, but the high-group component had only 20 selected points, below the primary minimum of 21. Displacement was therefore unevaluable under the main common-support rule (Supplementary Figure S1).

Reducing the side-count requirement to eight retained the low-group turn at 12.83 mm per 8 d and qualified a high-group turn at 9.57, giving an exploratory difference of −3.26 mm per 8 d. Both groups qualified in 596 of the 1,000 paired block draws. Within these eligible draws, the 2.5th, 50th and 97.5th displacement percentiles were −4.88, −2.28 and −0.65 mm per 8 d. The remaining 404 draws had no qualified pair. The sensitivity thus changed both the availability of a displacement estimate and the set of draws contributing to its conditional distribution.

Table 4. DSWI subgroup eligibility under the primary ten-points-per-side rule. Estimating displacement requires qualified turns in both groups on common support. Npre and Npost exclude the candidate. The 20-point high-wetness component falls below the 21-point minimum; N/A denotes an ineligible turn. Section 3.5 reports the post-hoc eight-point sensitivity.

Group	Domain	Qualified nodes	Selected points	Turn status	Turn (mm per 8 d)	N_{pre} / N_{post}
Low DSWI	Own	8,190	29	Qualified	12.83	12 / 16
High DSWI	Own	8,870	35	Qualified	21.29	24 / 10
Low DSWI	Common	8,128	29	Qualified	12.83	12 / 16
High DSWI	Common	8,128	20	Not qualified	N/A	N/A

4. Discussion

4.1. Persistent local boundaries and uncertain turning geometry

The local ET-conditioned VPD boundary persisted across both spline specifications and the alternative representations of native observations. All 1,000 block draws of the corrected weighted df6 fit recovered a boundary, and 72.6% met the expansion–contraction rule. The post-turn slope interval included zero in this fit and in the separate df7 analyses. Local sign changes were thus more consistent across the tested analyses than the direction of the longer boundary.

Reusing the spline training state restored predictions at matched coordinates and made the paired extraction comparison interpretable. Rebuilding the basis had changed the function represented by the archived coefficients. With prediction held consistent, differences between the two extractors could be traced to their support and curve-selection rules. This feature-specific check complements broader model-performance assessment (Gupta et al., 2012).

The recurring component identifies ET–VPD states where the fitted GPP association changes sign. Atmospheric dryness affects stomatal conductance, transpiration and photosynthesis across a wide range of soil-water conditions (Fu et al., 2022; Grossiord et al., 2020; Novick et al., 2016). Figures 4–5 place the component within its empirical support, with grey regions marking states that fell below the support criteria.

4.2. Native spatial support and coupled product structure

PML links GPP, canopy conductance and transpiration and includes VPD in its production calculations (Xu et al., 2026a; Y. Zhang et al., 2019). This coupling helps explain why both environmental variation and product structure contribute to the fitted response. Independent productivity observations would test how closely the recurring product boundary corresponds to vegetation behaviour.

The 200,000 assigned rows represented 21,491 PML cell–date records. Giving these records equal total fitting weight and reconstructing observations at PML-cell centres both retained the local component. Its occurrence was therefore insensitive to substantial changes in the influence of repeated source values. Figure 3 locates the native records and shows how often their predictor states entered qualified support.

Weighting changed fitting influence while retaining the nominal-record support mask. Single-record reconstruction changed the counting unit and the point used to assign meteorology. ERA5 cell×year resampling grouped shared forcing, whereas PML blocks grouped product histories. Both schemes consistently recovered local components in the weighted df7 analysis. Their intervals describe uncertainty on the retained grid and support; dependence between neighbouring cells and successive years extends beyond these block definitions (Cameron and Miller, 2015; Roberts et al., 2017).

4.3. The tradeoff between turn detection and location accuracy

Strict extraction located qualified true turns more accurately, but detected fewer genuine turns and accepted more turns on non-turning boundaries. Figure 7 makes this tradeoff visible by presenting location error beside detection rates. Judging the procedures on accepted locations alone would overlook the cases in which they missed or falsely identified a turn.

The high false-turn rate on horizontal boundaries exposes a weakness of the point qualification rule. Connectivity selects a coherent path, and the minimum side count supplies enough points for segmented fitting. The opposing-sign criterion can still accept small bends generated by noise because it imposes no minimum slope magnitude or slope-uncertainty requirement. Calibrating either requirement against known turning and non-turning responses is a useful next step for improving the extractor.

4.4. Implications for evaluating water–carbon response boundaries

Boundary assessment benefits from retaining native source identities and the spline training state. Support maps locate the predictor states available for extraction, grouped resampling measures variation in

geometry, and known-boundary experiments quantify detection performance. These checks make the sources of variation in the extracted curve easier to trace.

Common support directly affected the wetness-group comparison. The high-wetness component contained 20 points, leaving no eligible turn under the primary rule. Reducing the side-count requirement produced a displacement estimate, with both groups qualifying in 596/1,000 draws. That frequency specifies the subset represented by the displacement distribution. The P20 comparison likewise combined changes in sample composition and predictor coverage. Reporting eligibility beside turn estimates makes these comparisons easier to interpret.

Accessible data and executable instructions remain essential to reproducibility in computational hydrology (Hutton et al., 2016; Stagge et al., 2019). Derivative analyses also need the training basis, ordered prediction grid, native-unit identifiers and support mask. These objects preserve the evaluated function and its empirical context, allowing later studies to repeat the boundary comparison.

A repeatable boundary can guide the evaluation of water–carbon products in agricultural settings. It identifies states where the fitted association changes direction and where independent ET and productivity measurements would be particularly informative. Water-use assessments distinguish application, consumption and recoverable flows (Perry et al., 2009), while product suitability also depends on performance across crop growth stages (Stockle et al., 2025). Boundary analysis can help select the states for these evaluations.

4.5. Scope and further validation

The empirical assessment covers PML in Hetao over six years, with DSWI representing reanalysis deep-layer wetness. The simulations test four response families and three sampling conditions with coincident native and meteorological cells. Their deleted predictor band is narrow enough to be bridged by the support neighbourhood. The block intervals describe uncertainty conditional on the base support and spline state. Further validation should examine independent productivity observations, a wider range of response shapes and fully disconnected support, together with spatial and temporal dependence beyond the tested block definitions.

5. Conclusions

Local ET-conditioned VPD boundaries in Hetao persisted across alternative representations of native PML observations. The corrected weighted df6 fit recovered a boundary in all 1,000 block draws, with expansion–contraction geometry qualifying in 72.6%. The post-turn slope interval included zero, and the separate df7 analyses also yielded uncertain post-turn directions. The results establish the repeatability of a local boundary under the tested analyses and identify turning geometry as the more sensitive part of the response.

Experiments with known boundaries showed a tradeoff between location accuracy and detection. Strict extraction reduced location error among qualified true turns while increasing missed and false turns,

particularly on horizontal boundaries. In the wetness comparison, common support and side-count eligibility determined which turns could be compared. These findings show how reported transitions depend on both the fitted response and the procedure used to extract it.

Evaluating detection rates alongside conditional location accuracy and block uncertainty gives a more complete account of boundary reliability. Retaining native source identities and the spline prediction state makes that assessment reproducible. For gridded water–carbon products, the resulting local boundaries can guide further product evaluation while the estimated turns remain subject to uncertainty.

Funding

No funding was received for this manuscript.

References

Allen, R.G., Pereira, L.S., Raes, D., Smith, M., 1998. Crop evapotranspiration: Guidelines for computing crop water requirements. FAO Irrigation and Drainage Paper 56. FAO, Rome. https://www.fao.org/4/X0490E/x0490e00.htm

Cameron, A.C., Miller, D.L., 2015. A practitioner's guide to cluster-robust inference. Journal of Human Resources 50, 317–372. https://doi.org/10.3368/jhr.50.2.317

Feng, Z.-Z., Wang, X.-K., Feng, Z.-W., 2005. Soil N and salinity leaching after the autumn irrigation and its impact on groundwater in Hetao Irrigation District, China. Agricultural Water Management 71, 131–143. https://doi.org/10.1016/j.agwat.2004.07.001

Fu, Z., Ciais, P., Prentice, I.C., Gentine, P., Makowski, D., Bastos, A., Luo, X., Green, J.K., Stoy, P.C., Yang, H., Hajima, T., 2022. Atmospheric dryness reduces photosynthesis along a large range of soil water deficits. Nature Communications 13, 989. https://doi.org/10.1038/s41467-022-28652-7

Grossiord, C., Buckley, T.N., Cernusak, L.A., Novick, K.A., Poulter, B., Siegwolf, R.T.W., Sperry, J.S., McDowell, N.G., 2020. Plant responses to rising vapor pressure deficit. New Phytologist 226, 1550–1566. https://doi.org/10.1111/nph.16485

Gupta, H.V., Clark, M.P., Vrugt, J.A., Abramowitz, G., Ye, M., 2012. Towards a comprehensive assessment of model structural adequacy. Water Resources Research 48, W08301. https://doi.org/10.1029/2011WR011044

He, S., Zhang, Y., Ma, N., Tian, J., Kong, D., Liu, C., 2022. A daily and 500 m coupled evapotranspiration and gross primary production product across China during 2000–2020. Earth System Science Data 14, 5463–5488. https://doi.org/10.5194/essd-14-5463-2022

Hsiao, J., Swann, A.L.S., Kim, S.-H., 2019. Maize yield under a changing climate: The hidden role of vapor pressure deficit. Agricultural and Forest Meteorology 279, 107692. https://doi.org/10.1016/j.agrformet.2019.107692

Hutton, C., Wagener, T., Freer, J., Han, D., Duffy, C., Arheimer, B., 2016. Most computational hydrology is not reproducible, so is it really science? Water Resources Research 52, 7548–7555. https://doi.org/10.1002/2016WR019285

Liu, L., Gudmundsson, L., Hauser, M., Qin, D., Li, S., Seneviratne, S.I., 2020. Soil moisture dominates dryness stress on ecosystem production globally. Nature Communications 11, 4892. https://doi.org/10.1038/s41467-020-18631-1

Massmann, A., Gentine, P., Lin, C., 2019. When Does Vapor Pressure Deficit Drive or Reduce Evapotranspiration? Journal of Advances in Modeling Earth Systems 11, 3305–3320. https://doi.org/10.1029/2019MS001790

Mu, Q., Zhao, M., Running, S.W., 2011. Improvements to a MODIS global terrestrial evapotranspiration algorithm. Remote Sensing of Environment 115, 1781–1800. https://doi.org/10.1016/j.rse.2011.02.019

Muñoz-Sabater, J., Dutra, E., Agustí-Panareda, A., Albergel, C., Arduini, G., Balsamo, G., Boussetta, S., Choulga, M., Harrigan, S., Hersbach, H., Martens, B., Miralles, D.G., Piles, M., Rodríguez-Fernández, N.J., Zsoter, E., Buontempo, C., Thépaut, J.-N., 2021. ERA5-Land: a state-of-the-art global reanalysis dataset for land applications. Earth System Science Data 13, 4349–4383. https://doi.org/10.5194/essd-13-4349-2021

Novick, K.A., Ficklin, D.L., Stoy, P.C., Williams, C.A., Bohrer, G., Oishi, A.C., Papuga, S.A., Blanken, P.D., Noormets, A., Sulman, B.N., Scott, R.L., Wang, L., Phillips, R.P., 2016. The increasing importance of atmospheric demand for ecosystem water and carbon fluxes. Nature Climate Change 6, 1023–1027. https://doi.org/10.1038/nclimate3114

Patsy developers, n.d. Spline regression. Patsy documentation. https://patsy.readthedocs.io/en/latest/spline-regression.html (accessed 6 October 2026).

Perry, C., Steduto, P., Allen, R.G., Burt, C.M., 2009. Increasing productivity in irrigated agriculture: Agronomic constraints and hydrological realities. Agricultural Water Management 96, 1517–1524. https://doi.org/10.1016/j.agwat.2009.05.005

Ramos, T.B., Liu, M., Paredes, P., Shi, H., Feng, Z., Lei, H., Pereira, L.S., 2023. Salts dynamics in maize irrigation in the Hetao plateau using static water table lysimeters and HYDRUS-1D with focus on the autumn leaching irrigation. Agricultural Water Management 283, 108306. https://doi.org/10.1016/j.agwat.2023.108306

Roberts, D.R., Bahn, V., Ciuti, S., Boyce, M.S., Elith, J., Guillera-Arroita, G., Hauenstein, S., Lahoz-Monfort, J.J., Schröder, B., Thuiller, W., Warton, D.I., Wintle, B.A., Hartig, F., Dormann, C.F., 2017. Cross-validation strategies for data with temporal, spatial, hierarchical, or phylogenetic structure. Ecography 40, 913–929. https://doi.org/10.1111/ecog.02881

Stagge, J.H., Rosenberg, D.E., Abdallah, A.M., Akbar, H., Attallah, N.A., James, R., 2019. Assessing data availability and research reproducibility in hydrology and water resources. Scientific Data 6, 190030. https://doi.org/10.1038/sdata.2019.30

Stockle, C.O., Liu, M., Kadam, S.A., Evett, S.R., Marek, G.W., Colaizzi, P.D., 2025. Comparing evapotranspiration estimations using crop model-data fusion and satellite data-based models with lysimetric observations: Implications for irrigation scheduling. Agricultural Water Management 311, 109372. https://doi.org/10.1016/j.agwat.2025.109372

Wood, S.N., 2017. Generalized Additive Models: An Introduction with R, 2nd ed. Chapman and Hall/CRC. https://doi.org/10.1201/9781315370279

Xiao, X., Hollinger, D., Aber, J., Goltz, M., Davidson, E.A., Zhang, Q., Moore, B., 2004. Satellite-based modeling of gross primary production in an evergreen needleleaf forest. Remote Sensing of Environment 89, 519–534. https://doi.org/10.1016/j.rse.2003.11.008

Xu, Z., Zhang, Y., Kong, D., 2026b. PML-V2.2: Global terrestrial evapotranspiration and gross primary production dataset from 1982 to near present [data set]. National Tibetan Plateau / Third Pole Environment Data Center. https://doi.org/10.11888/Terre.tpdc.303314

Xu, Z., Zhang, Y., Kong, D., Ma, N., Zhang, X., 2026a. Extended global terrestrial evapotranspiration and gross primary production dataset from 1982 to near present. Earth System Science Data 18, 5663–5695. https://doi.org/10.5194/essd-18-5663-2026

Yang, J., Huang, X., 2021. The 30 m annual land cover dataset and its dynamics in China from 1990 to 2019. Earth System Science Data 13, 3907–3925. https://doi.org/10.5194/essd-13-3907-2021

Yang, J., Huang, X., 2025. The 30 m annual land cover datasets and its dynamics in China from 1985 to 2024, version 1.0.4 [data set]. Zenodo. https://doi.org/10.5281/zenodo.15853565

Yu, R., Liu, T., Xu, Y., Zhu, C., Zhang, Q., Qu, Z., Liu, X., Li, C., 2010. Analysis of salinization dynamics by remote sensing in Hetao Irrigation District of North China. Agricultural Water Management 97, 1952–1960. https://doi.org/10.1016/j.agwat.2010.03.009

Yuan, W., Zheng, Y., Piao, S., Ciais, P., Lombardozzi, D., Wang, Y., Ryu, Y., Chen, G., Dong, W., Hu, Z., Jain, A.K., Jiang, C., Kato, E., Li, S., Lienert, S., Liu, S., Nabel, J.E.M.S., Qin, Z., Quine, T., Sitch, S., Smith, W.K., Wang, F., Wu, C., Xiao, Z., Yang, S., 2019. Increased atmospheric vapor pressure deficit reduces global vegetation growth. Science Advances 5, eaax1396. https://doi.org/10.1126/sciadv.aax1396

Zhang, Q., Ficklin, D.L., Manzoni, S., Wang, L., Way, D., Phillips, R.P., Novick, K.A., 2019. Response of ecosystem intrinsic water use efficiency and gross primary productivity to rising vapor pressure deficit. Environmental Research Letters 14, 074023. https://doi.org/10.1088/1748-9326/ab2603

Zhang, Y., Kong, D., Gan, R., Chiew, F.H.S., McVicar, T.R., Zhang, Q., Yang, Y., 2019. Coupled estimation of 500 m and 8-day resolution global evapotranspiration and gross primary production in 2002–2017. Remote Sensing of Environment 222, 165–182. https://doi.org/10.1016/j.rse.2018.12.031

Supplementary Files

This is a list of supplementary files associated with this preprint. Click to download.

- SupplementaryMaterial20261025.docx